# FINAL REPORT

| | | | |
|---|---|---|---|
| **FFG Projektnummer** | 878151 | **FörderungsnehmerIn** | ÖBV |
| **Bericht Nr.** | 1 | **Berichtszeitraum** | 01.10.2021 – 30.09.2022 |
| **Bericht erstellt von** | Pauser, Robisson | | |

***Richtwert für den Umfang: 10-20 Seiten***

## 1. Ziele und Ergebnisse

- Wurden die dem Förderungsvertrag zugrunde liegenden Ziele erreicht? Sind diese Ziele noch aktuell bzw. realistisch? Achtung: Änderungen von Zielen erfordern eine Genehmigung durch die FFG.
- Vergleichen Sie die Ziele mit den erreichten Ergebnissen.
- Beschreiben Sie „Highlights" und aufgetretene Probleme bei der Zielerreichung.

This fourth year project achievements include:

- The rheological characterization of an alkali-activated binder (AAB) under flow, quantifying its yield stress. Observations of the sample in between the two parallel plates of the rheometer show that the AAB slurry tends to localize strain under flow, similarly to Portland cement slurries.
- The precise characterization of early reactivity of gypsum/cement mixtures and the potential formation of secondary ettringite was performed using (in-situ) X-ray powder diffraction (XRPD) measurements, coupled with pH and heat of hydration (calorimetry) evaluations. Cement mixtures were chosen from low aluminate content to high aluminate targeting the understanding of the mechanisms of internal sulfate attacks (ISA).
- The development of a 3D numerical model to predict damage linked to drying shrinkage in sloped floors.
- The design and characterization of concretes made of recycled concretes (fresh state).
- The mechanical characterization of hardened AAB and lightweight concrete made with expanded clay beads.

Specific work packages are described in section 2.2 with project abstracts in the next pages. The work packages are incorporated into the 4 sub-projects (1. Internal sulfate attack: An issue in recycled aggregate concretes, 2. Yield stress of cement paste & AAB and determination of local flow heterogeneities by imaging, 3. Sustainable concrete: alkali activated binders, recycled concrete binder and lightweight concrete using expanded clay aggregates, 4. Interfaces: Bond strength in sloped floors and influence of angle on failure due to drying shrinkage).

The team (co-authors of reports) is composed of Dana Daneshvar, Karl Deix, Subhransu Dhar, Johannes Kirnbauer, Teresa Liberto and Agathe Robisson.

# Projekt 1: Interner Sulfatangriff: Ein Problem bei rezyklierten Gesteinskörnungen (RGK)? (AP5, AP7, AP9)

Teresa Liberto, Johannes Kirnbauer, Agathe Robisson

## Zusammenfassung

Die Untersuchung des internen Sulfatangriffs (ISA) ist von grundlegender Bedeutung für die Verwendung von Recyclingbeton (RC) als Zuschlagstoffe in neuen zementgebundenen Formulierungen. Tatsächlich können diese recycelten Zuschlagstoffe einen Überschuss an Gips enthalten, der die festgelegte Betonstruktur im Laufe der Zeit beschädigen kann.
Angesichts der extremen Komplexität dieser Systeme untersuchten wir hier die chemischen Prozesse, die zur Bildung von sekundärem Ettringit für zwei Zementtypen führen, einen aluminatreichen (Ciment Fondue) und den anderen aluminatarmen (Der Contragress). Die beiden hydratisierten Zemente (hydratisierter Fondue HF und hydratisierter Contragress HC) wurden mit und ohne einem Überschuss an Gips (hydratisierter Gips HG) charakterisiert, um die Bildung von sekundärem Ettringit durch Röntgenpulverbeugung (XRPD), Kalorimetrie und pH-Messungen zu messen. Die Ergebnisse zeigen die schnelle Ausfällung von sekundärem Ettringit in HF+HG, beginnend unmittelbar nach dem Kontakt mit Wasser bis zu 24 h. Der HC hingegen zeigt eine geringere und langsamere sekundäre Ettringitbildung mit möglichen langfristigen Anstiegen.

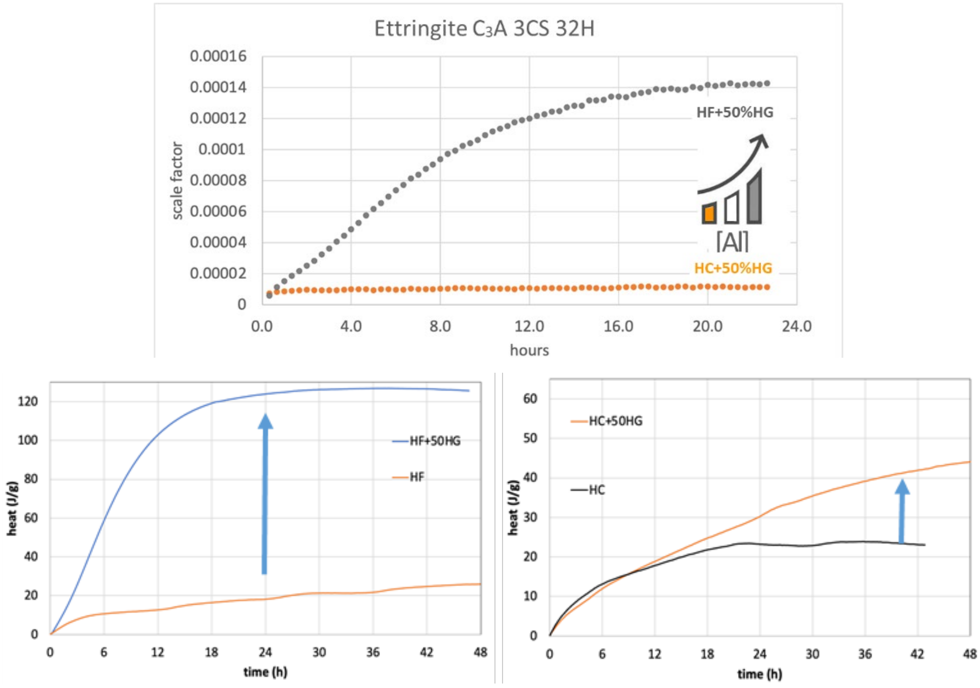


Es wurden auch Expansionsmessungen durchgeführt. Sowohl 2 Jahre alte als auch kürzlich vorbereitete Fondu-Prismen sowie 2 Jahre alte Der Blaue-Proben wurden getestet und zeigten keine Ausdehnung. Das Ring-Setup von Le-Chatelier wurde modifiziert, aber es konnten trotzdem keine befriedigenden qualitative Ergebnisse erzielt werden. Die Tests bei erhöhten Temperaturen mit einem Oedometer schlugen ebenfalls fehl, was zu unzuverlässigen Messungen mit allen getesteten Kalibriermaterialien führte. Um die Mängel der letzten beiden Techniken zu überwinden, haben wir uns entschieden, einen Versuchsaufbau zur Messung des Quelldruckes von Grund auf neu zu entwickeln.

# Projekt 2: Fließspannung von Zementpaste & AAB und Bestimmung lokaler Strömungsheterogenitäten durch Bildgebung (AP3)

Subransu Dhar, Teresa Liberto, Agathe Robisson

## Zusammenfassung

Die anziehenden Wechselwirkungskräfte zwischen gewöhnlichen Portlandzementpartikeln (OPC) und zwischen alkaliaktivierten Bindemittelpartikeln (AAB) nehmen mit der Zeit zu, was zur Aushärtung des Materials führt. Im frischen (flüssigen oder pastösen) Zustand sind diese Anziehungskräfte für die Entwicklung einer Streckgrenze im Ruhezustand verantwortlich. Hier wollen wir die Fließspannung eines AAB-Leimes mit verschiedenen Methoden messen und diese Werte mit Werten vergleichen, die von Messungen von OPC-Leimen erhalten wurden (Vorjahresergebnisse). Die mit der Vane-Geometrie bei einem w/b-Verhältnis von 0,4 erhaltenen Fließspannungen sind ziemlich ähnlich: 158 Pa für OPC und 202 Pa für AAB. Vergleicht man die mit allen Geometrien erzielten Ergebnisse, so sind die mit Parallelplatten- und Couette-Geometrien gemessenen Fließspannungen wiederum viel niedriger als die Werte, die mit den Vane- und Helix-Geometrien oder mit dem Mini-Kegel-Slump-Test erzielt wurden, wie es bei OPC der Fall war. Dies zeigt tendenziell eine gewisse Ähnlichkeit in den Fließeigenschaften von OPC und AAB.
Die Quelle der fehlerhaften Ergebnisse, die mit der Parallelplatten-Geometrie und den Couette-Geometrien erzielt wurden, wurde untersucht, indem die Probe innerhalb der Parallelplatten-Geometrie abgebildet wurde. Die Ergebnisse zeigen, dass die Probe nicht innerhalb des gesamten Spalts geschert wird, sondern ein Teil der Probe in der Nähe der festen Bodenplatte statisch bleibt. Die Höhe der Probe, die innerhalb des Spalts geschert wird, wurde quantifiziert und nimmt mit der Scherrate zu, erreicht aber bei der maximalen getesteten Scherrate (300 $s^{-1}$) nie den vollen Spalt. Diese Beobachtung kann jedoch nicht den sehr niedrigen Wert erklären, der mit der Parallelplatten-Geometrie erzielt wurde, und erfordert mehr Arbeit, einschließlich der Quantifizierung des Geschwindigkeitsprofils durch Partikelbildvelocimetrie (PIV), ein Ziel für das nächste Jahr.

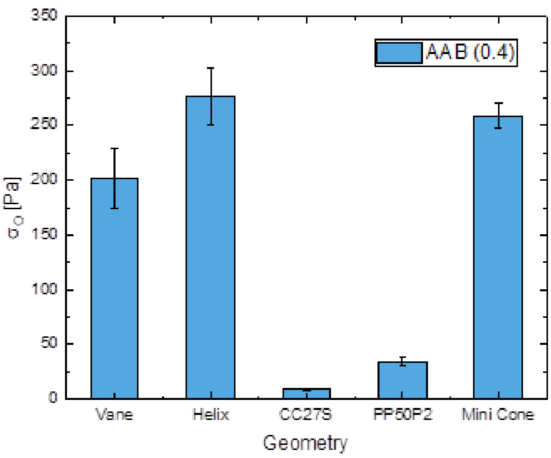


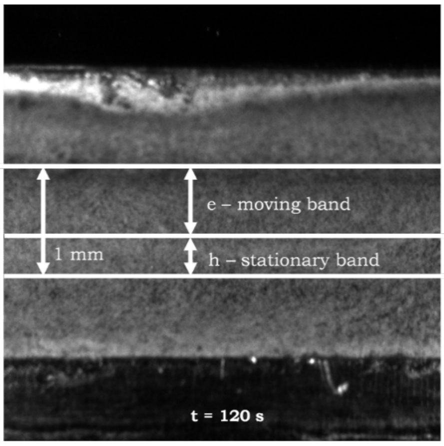

# Projekt 3: Nachhaltiger Beton: alkaliaktivierte Bindemittel, Recyclingbetonbindemittel und Leichtbeton mit Blähtonzuschlagstoffen (AP5, AP7, AP9)

Teresa Liberto, Dana Daneshvar, Johannes Kirnbauer, Agathe Robisson

## Zusammenfassung

Die Untersuchung von nachhaltigem Beton erstreckt sich über verschiedene zementgebundene Materialien: alkaliaktivierte Bindemittel (AAB), Recyclingbeton und leichter Blähtonbeton.
Wir haben in unseren früheren Studien die unterschiedliche chemische Zusammensetzung von AAB im Vergleich zu OPC hervorgehoben und die Eigenschaften in frischem Zustand (Verarbeitbarkeit) durch Zugabe von Calciumionen (über CaCl2) und Fließmittel (PCE) verbessert. Die positiven Auswirkungen dieser Zusätze auf die Verarbeitbarkeit von AAB-Leimen veranlassten uns, die Eigenschaften von festen AAB-Mörteln zu untersuchen. In diesem Bericht zeigen wir das Druckfestigkeitsverhalten unseres optimierten AAB-Mörtels bei unterschiedlichen Wasser/Bindemittel-Verhältnissen (w/b) und Lagerbedingungen. Die erzielten Ergebnisse sind vielversprechend für den Einsatz von AAB in Niedriglastanwendungen.

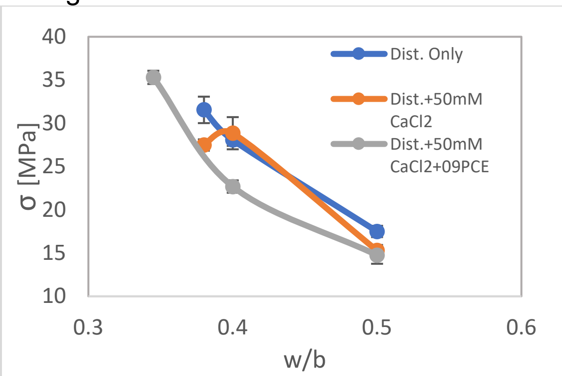


Der Bericht beschreibt auch die Entwicklung von Beton aus gemahlenem Recyclingbeton als Zuschlagstoffersatz, wobei die Mischungen eine ähnliche Verarbeitbarkeit aufweisen.
Leichtbeton mit einer großen Menge an Blähton bietet das Potenzial, sowohl Beton mit niedrigem OPC-Gehalt als auch Wärmedämmbeton herzustellen. In diesem Jahr haben wir einen Basisbeton getestet, der als Grundlage für zukünftige Optimierungen verwendet werden kann (die niedrigste Dichte, die während dieser Vorversuche erreicht wurde, betrug 1018 kg/m³).

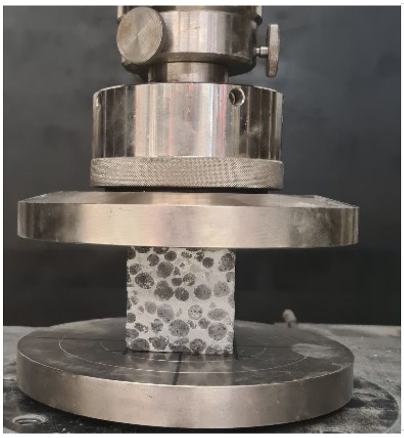

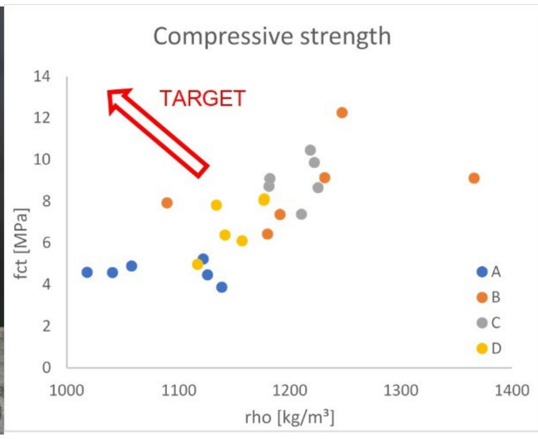

## Projekt 4: Schnittstellen: Haftfestigkeit in geneigten Böden und Einfluss des Winkels auf das Versagen aufgrund von Trocknungsschrumpfung. (AP6)

D. Daneshvar, K. Deix, A. Robisson


### Zusammenfassung

Mehrschichtige Betonsysteme wurden häufig in Brückendecks, Betondecke und Estriche eingesetzt. Das behinderte Trocknungsschwinden des Overlays ist sehr besorgniserregend, da sie zu Overlay-Rissen und/oder Grenzflächenablösungen führen kann. Bei solchen Konstruktionen wird typischerweise davon ausgegangen, dass ein Querneigung das Oberflächenwasser ableitet. Trotz der Fortschritte beim Verständnis des Trocknungsschwindens von nicht geneigten Beton-Beton-Verbundwerkstoffen gibt es immer noch Fragen hinsichtlich der Überlagerungsrissbildung sowie des Verbundversagens in geneigten Beton-Beton-Verbundwerkstoffen. Die aktuelle Studie etabliert ein High-Fidelity-Berechnungsmodell, das mit experimentellen Tests validiert wurde, um die strukturelle Leistung von geneigten, doppellagigen Overlay-Systemen unter Trocknungsschwinden zu bewerten. Die Simulationsszenarien decken systematisch die Auswirkungen wichtiger Overlay-Eigenschaften und Grenzflächenbedingungen ab. Die Ergebnisse der numerischen Analyse zeigen die kritische Rolle der Overlay-Dicke und der mechanischen Eigenschaften in der Zeit von Overlay-Cracking- und Grenzflächen-Ablösungsfehlern. Basierend auf den erhaltenen Ergebnissen kann die Implementierung einer Querneigung die Ausfälle je nach Anfangsdicke verzögern. Eine höhere Grenzflächensteifigkeit induziert auch eine stärkere Zurückhaltung gegenüber der Überlagerungsschrumpfung, was zu einer schnelleren Überlagerungsrissbildung führt.


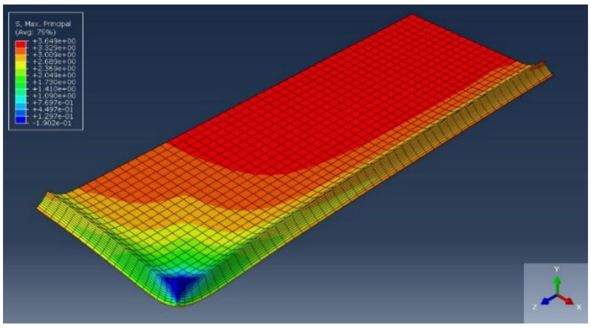


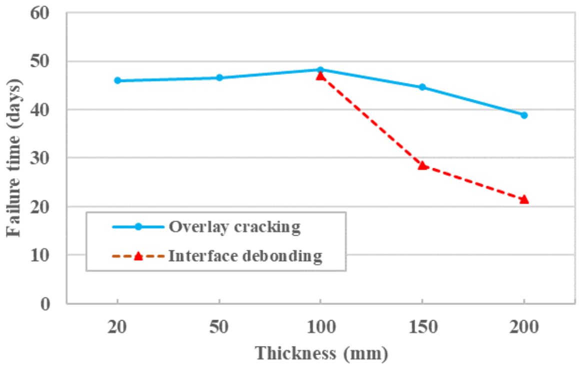

# 2. Arbeitspakete und Meilensteine

## 2.1 Übersichtstabellen

***Erläuterung:***
Die Tabellen sind analog zum Förderungsansuchen aufgebaut.
Basistermin: Termin laut Förderungsansuchen bzw. laut Vertrag gültigem Projektplan
Aktuelle Planung: Termin laut zum Zeitpunkt der Berichtslegung gültiger Planung

**Tabelle 1: Arbeitspakete**

| AP No. | work package designation | Degree of completion | base date | | Current | | Achieved results / deviations |
|---|---|---|---|---|---|---|---|
| | | | start | end | start | end | |
| 1 | Project management | 40% | 10.18 | 09.23 | 10.18 | 09.23 | Mid-year 4 meeting held 12.05.2022 at TU Wien. End of year 4 meeting planned 28.09.2021. |
| 2 | State of the art | 90% | 10.18 | 09.19 | 10.18 | 09.23 | Examination of EU legislation for recyclability in construction, foam cement, durability of recycled aggregate concrete continues with each step of the research projects. |
| 3 | Entwicklung rheologischer Prüfungen und Verfahren<br><br>Development of rheological tests and procedures | 90% | 10.18 | 09.21 | 10.18 | 09.23 | We have shown evidence that the parallel plate geometry does not shear the whole cement paste. We measured the width of the stationary gap as a function of shear rate and have shown a dependance. Results also showed that alkali-activated binders seem to flow similarly to ordinary Portland cement. |
| 4 | Untersuchung des Einflusses des Misch-vorgangs<br><br>Investigation of the influence of the mixing process | 100% | 10.18 | 09.21 | 10.18 | 09.21 | Fertiggestellt. |
| 5 | Einfluss der Ze-mentpartikelgrößen-verteilung und beschaffenheit (Vorhandensein von nachhaltigen Bindemitteln) auf die Betonrheologie, die | 90% | 10.18 | 09.20 | 10.18 | 09.23 | Alkali-activated mortars were characterized in their set state. X-ray diffraction and calorimetry analysis of mixtures of gypsum and cements with various initial content of aluminum were performed and results analyzed in comparison with early reactivity of gypsum/cement mixtures by SAOS and Le-Chatelier rings. Prisms of Ciment Fondu and |

| | | | | | | | |
|---|---|---|---|---|---|---|---|
| | Schäumbarkeit, und das Erstarrungsverhalten<br><br>Influence of cement particle size distribution and nature (presence of sustainable binders) on concrete rheology, foamability, and setting properties | | | | | | excess gypsum exhibited no expansion after a few months. |
| 6 | Schnittstellen zwischen alten Material und neuem Beton<br><br>Interfaces between old material and new concrete | 90% | 10.18 | 09.23 | 10.18 | 09.**23** | This year was spent establishing a full 3D model of a sloped floor using finite element analysis (FEA) model rather than performing an experimental characterization. This theoretical prediction is a preliminary study to select the sloped floor geome-tries for the experimental campaign. Conditions for this limited series of tests will therefore be identified from the computational results. |
| 7 | Einrichtung zur Messung der Infiltration<br><br>Device for the measurement of infiltration | 60% | 10.19 | 10.22 | 07.20 | 10.23 | Light weight concrete samples manufactured with the non-optimized pouring process were tested in their hardened state: The density of samples ranges from 1018 to 1366 kg/$m^3$ and the compressive strength from 3.9 to 12.3 MPa, exhibiting large variability. The samples manufactured with infiltration device were not characterized as the device requires improvements. |
| 8 | Equipment for the production of cement foams | 100% / stopped | 10.19 | 10.20 | 10.19 | 10.20 | Stopped |
| 9 | Device for characterizing volume changes or limiting pressure of RA concretes | 60% | 10.19 | 10.23 | 10.19 | 10.23 | The upgrade of the geotechnic oedometer could not be achieved due to unexplained lack of stability of the device above room T. A design concept was decided afresh.<br>Le-Chatelier free expansion measurements were only successful on compounds that expanded by a large factor.<br>High-performance concrete (HPC) prepared with recycled |

| | | | | | | | |
|---|---|---|---|---|---|---|---|
| | | | | | | | aggregates were prepared and characterized in their fresh state. |
| 10 | High thermal insulation in a double walled tower | 0% | 10.22 | 10.23 | 10.22 | 10.23 | This work package starts in the last year of research |

## 2.2 Description of the work carried out during the reporting period

### AP 3: Development of rheological tests and procedures

#### Motivation

In the last report, we reported important differences in the measured values of the yield stress of an ordinary Portland cement paste using various rheometer geometries and a cone spread test. The yield stresses measured with the plate-plate and concentric cylinder (Couette) geometries were significantly lower as compared to other geometries. This year, a similar study was performed on an alkali activated binder (AAB). Besides supporting the development of proper rheological protocols, this work helped us evaluate if the AAB paste has a similar ability to localize strain during flow as OPC.
Additionally, in order to further investigate the cause behind the difference between the measured yield stresses, an imaging setup was adapted to the rheometer with the parallel plate geometry. A high-speed camera, equipped with a magnifying lens was used to image the gap between the parallel plates. The images revealed the formation of different regions in cement paste under shear. The lower region (near the static bottom plate) appeared non-moving, indicating that the cement was not sheared. This year results quantify how the width of the moving band changes with the imposed angular velocity.

#### Materials and methods

As ordinary Portland cement (OPC), Contragress cement powder 42.5 R-SR 0 WT 27 $C_3A$-free from Lafarge-Holcim was used. The alkali activated binder (AAB) consists of 91.5 % of slag (Ecocem, France), 5 % of $NaCO_3$, and 3.5 % of $Ca(OH)_2$ (Purdon, Patent 1935). For both materials, the powder was dispersed in distilled water with a water/binder (w/b) ratio of 0.4, using either an ultra-turrax mixer (IKA) to produce 10 ml of sample (OPC), or an overhead stirrer (IKA) to prepare 50 ml of the sample (AAB). The mixing consisted of three steps. Step I: the paste was mixed at 6000 rpm for 3 minutes; Step II: the sample was kept at rest for 10 mins; Step III: the cement paste was further mixed for 1 minute at the same speed and was used for experiments. All the experiments were repeated two times and the temperature was controlled at 20 °C for the experiments performed on the rheometer and room temperature for the cone spread test.

#### Experimental protocol

<u>The yield stress measurement of AAB:</u> Once the sample was mixed, it was instantly loaded to the rheometer or used for mini-cone slump test. A stress decreasing logarithmically with time, from high to a low value, was imposed, while the shear rate was recorded. The yield stress $\tau_0$ is chosen as the stress point corresponding to the shear rate value decreasing below 1 $s^{-1}$.

The yield stress of the paste was also measured using mini-cone slump test, as described in previous report.

Imaging of OPC paste in parallel plate geometry: The sample was loaded between the parallel plates soon after the mixing protocol was completed. We used serrated parallel plates of diameter 50 mm and the gap between the plates was maintained at 1 mm. The camera lens was focussed at the edge of the plates and the sample at the boundary of the plates was imaged. Five different angular velocities to the top plate were imposed (0.06, 0.6, 3, 6, 18 and 300 rad/s$^{-1}$). The width of the moving band e at 120 s (after start of shear) was recorded (see Fig 3.1). The stationary band is depicted as 'h'.

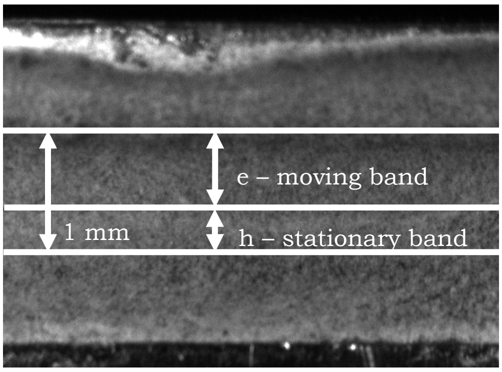


*Fig 3.1  An image of OPC paste at the edge of the plates, under shear after 120 s. The horizontal white lines are used to highlight the boundary of the stationary and moving bands.*

**Results and discussions**

Measured yield stress with different geometries in the case of AAB:  Fig. 3.2 shows the results of the yield stresses measured using several geometries and mini-cone slump test.

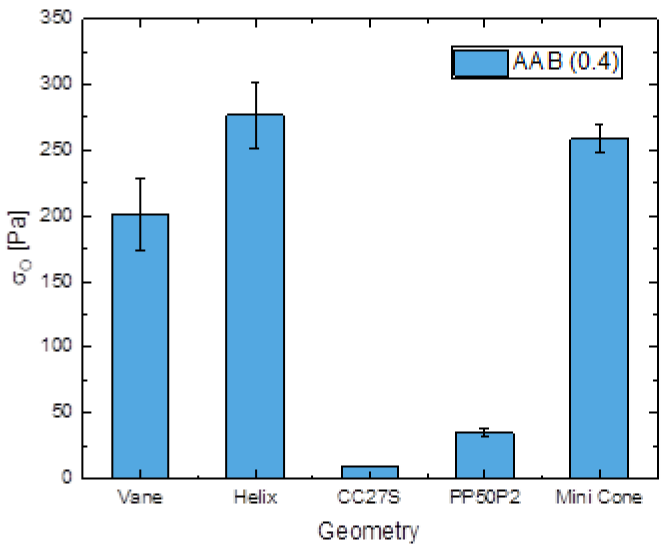


*Fig 3.2 Histogram showing the yield stress of an AAB paste at w/b=0.4 measured using different geometries. The error bars represent the difference between two tests.*

Results show that the yield stresses measured using the plate-plate and the Couette geometries are much smaller (by more than one order of magnitude) than the values obtained with the vane and helix geometries and from spread. These pattern of results matches the results obtained with ordinary Portland cement, shown last year.

<u>Measurement of band width with imposed angular velocity in OPC paste</u>: In Fig 3.3, the moving band width e is plotted as a function of the imposed angular velocity of the top plate Ω.

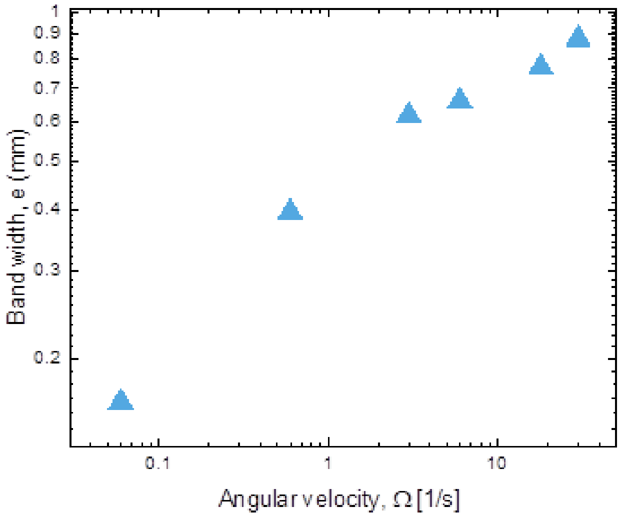


*Fig 3.3 Graph showing the variation of width of moving band 'e' (in mm) with the imposed angular velocity Ω (in $s^{-1}$) to the top plate for an OPC paste (w/b=0.4).*

Results clearly show that the width of the moving band e depends upon the imposed angular velocity Ω, and e increases with Ω. A similar result was obtained by [3], where non-Brownian particles were dispersed in a Newtonian fluid with a density difference.

### Conclusions

A comparative study of the flow properties of AAB and cement, leading to the measurement of the yield stress, shows that both cement and AAB seem to localize shear, leading to erroneous measurements of the yield stress in parallel plate and concentric cylinder geometries.

These results motivated the use of an imaging system connected to the rheometer to image the flow of the paste placed in between the parallel plate geometry. Results show the presence of heterogeneities in the flow, where only a part of the sample is sheared. Also, the width of the moving gap was shown to depend upon the applied angular velocity of the top moving plate.

### References:


[1] N Roussel and Ph Coussot. "Fifty-cent rheometer" for yield stress measurements: from slump to spreading flow. Journal of rheology, 49(3):705–718, 2005.

[2] Zhijun Tan, Susan A Bernal, and John L Provis. Reproducible mini-slump test procedure for measuring the yield stress of cementitious pastes. Materials and Structures, 50(6):1–12, 2017.

[3] C Barentin, E Azanza, and B Pouligny. Flow and segregation in sheared granular slurries. Europhysics Letters (EPL), 66(1):139–145, April 2004.

## AP 5: Influence of cement particle size distribution and nature (presence of sustainable binders) on concrete rheology, foamability, and setting properties

### Early reactivity of gypsum/cement mixtures: role of aluminum content on formation of secondary ettringite

Understanding the mechanisms responsible for the formation of secondary ettringite in recycled concrete (RC) is a difficult task due to the complexity of the reactions involved. In our previous report (3rd year, WP5+WP9), the basics of sulfate attack (with a special focus on the internal sulfate attacks -ISA-) were summarized, together with attempts to quantify the expansion in gypsum/cement mixtures linked to the formation of secondary ettringite. In particular, SAOS measurements have shown the complexity of the behavior of these systems and suggested additional tests for a better interpretation. Here, in order to quantify the early reactivity of gypsum/cement mixtures and the potential formation of ettringite, X-ray powder diffraction (XRPD) measurements were coupled with pH and heat of hydration evaluations.

Materials and Methods

In this study, we selected two cement types: one aluminum-rich (Ciment Fondu) and one aluminum-poor (Der Contragress, $C_3A$-free). In order to accelerate the formation of secondary ettringite, both cements were previously hydrated, as detailed in the 3$^{rd}$ year report (WP5+WP9).

The hydrated powders were characterized via XRPD to define their chemical composition. In order to follow the evolution of their phases after the hydrated powder-water contact, in-situ XRPD measurements were made. To accelerate the secondary ettringite formation, the HF and HC pastes were prepared at a water to hydrate cement ratio (w/c) of 0.6 and by adding 50% of hydrated gypsum (HG).

The pH evolution of HF and HC suspensions (w/c=2), with and without 50%HG was measured for 4 H under magnetic stirring.

Calorimetry measurements were also performed for HF and HC pastes with and without 50%HG at a w/c=0.5 and 0.4, respectively.

Results and Discussion

The two hydrated powders were tested via XRPD to quantify the exact amount by weight of their constituent phases, as reported in Tab. 5.1.

This analysis confirms the higher amount of aluminate phases present in HF compared to HC.
In order to form secondary ettringite, a source of aluminum is needed together with the added source of sulfate (HG). Fig. 5.1 shows the trend for the more relevant phases of the HF+50%HG paste (w/c=0.6) in time (~1 day). These plots have a scale factor as y-axis. In these in-situ measurements, we cannot add any internal standard (as possible for the powder) to quantify the weight percentage, as it would interfere with the hydration reaction.

| Phase Name | Wt% |
|---|---|
| $C_3A$+$C_4AF$ | 7 |
| Hydrogarnet ($C_3AH_6$) | 38 |
| Gibbsite ($AH_3$) | 17 |
| CA | 4 |
| Magnetite ($Fe_3O_4$) | 4 |
| $C_2AS$ | 2 |
| Am-unkn | 28 |

| Phase Name | Wt% |
|---|---|
| $C_3S$+$C_2S$ | 13 |
| $C_4AF$ | 6 |
| Ettringite | 4 |
| Portlandite (CH) | 14 |
| Calcite | 4 |
| Am-unkn | 59 |

*Tab. 5.1 Rietveld quantitative phase analysis with internal standard (10% of zincite ZnO). Left: Hydrated Fondue (HF). Right: hydrated Contragress (HC). Am-Unkn stands for amorphous and unknown phases that cannot be detected by XRPD due to their low crystallinity.*

The main aluminum sources are CA and hydrogarnet ($C_3AH_6$), which combined with the HG bring to a massive formation of secondary ettringite over the first day of hydration. Analogously, Fig. 5.2 shows the evolution of the phases for the HC+50HG paste at w/c=0.6.

In this case, we expect $C_4AF$ to be the main aluminum source, but it stays constant for the first day of testing. This is attributed to its very slow dissolution in comparison to other aluminate phases. The modest formation of ettringite is then hypothetically due to the aluminum present in the $C_3S$ as an impurity. The overall gypsum content does not vary much (not shown), and the portlandite (CH) slightly increases. These results suggest that the formation of ettringite due to the reaction between $C_4AF$ and HG is slow, as observed in real cases of damaged structures due to ISA (i.e., years).

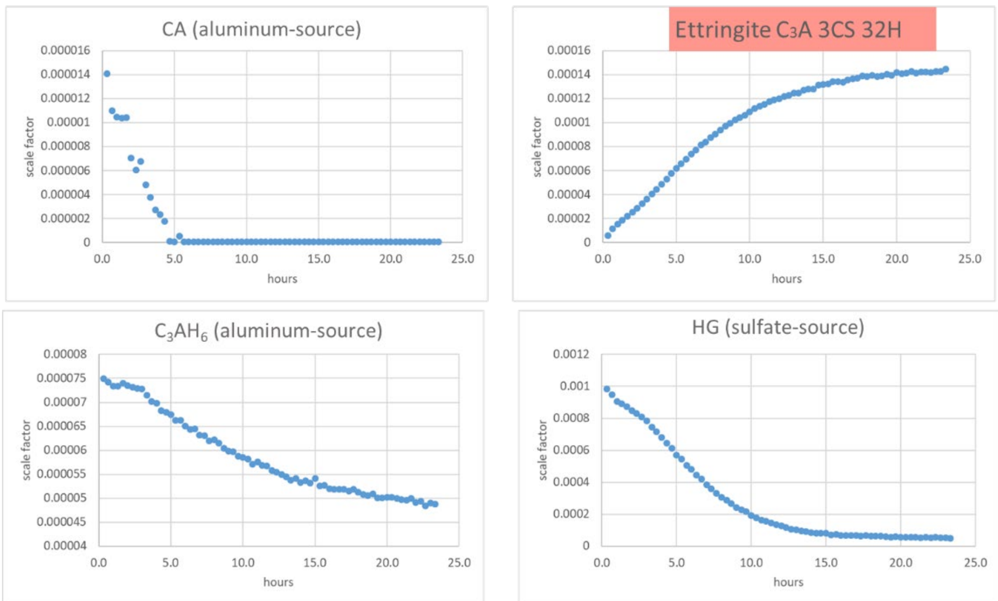


*Fig. 5.1 Scale factor versus time for the main constituent phases of the HF+50%HG paste at a w/c=0.6. Gibbsite ($AH_3$) is constant in time and $C_3A$ is below the detection limit.*

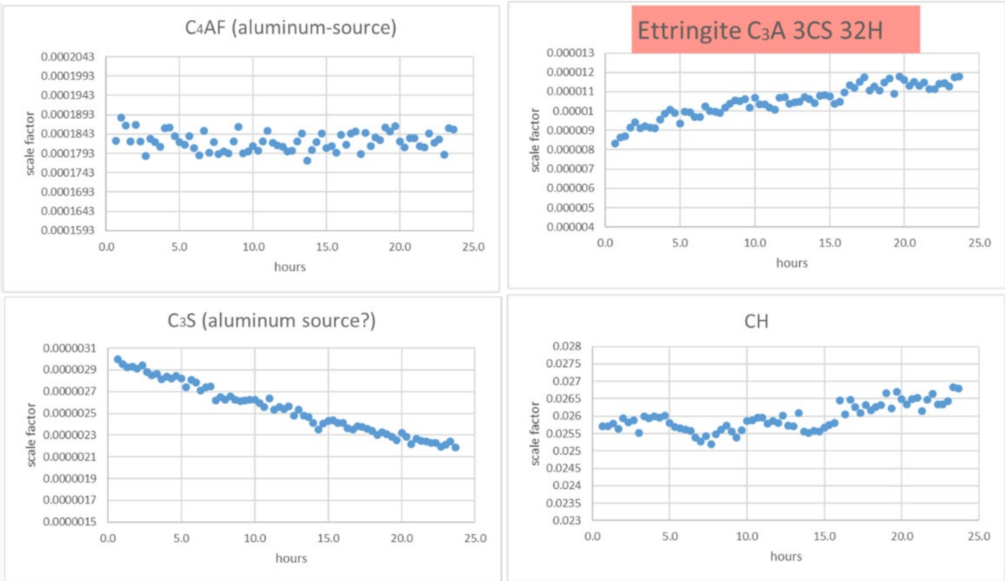


*Fig.5.2 Scale factor versus time for the main constituent phases of the HC+50%HG paste at a w/c=0.6. Monoclinic $C_3S$ can contain aluminum concurring in forming ettringite.*

The trend observed with XRPD measurements is also confirmed by pH (Fig. 5.3) and calorimetry (Fig.5.4) ones.

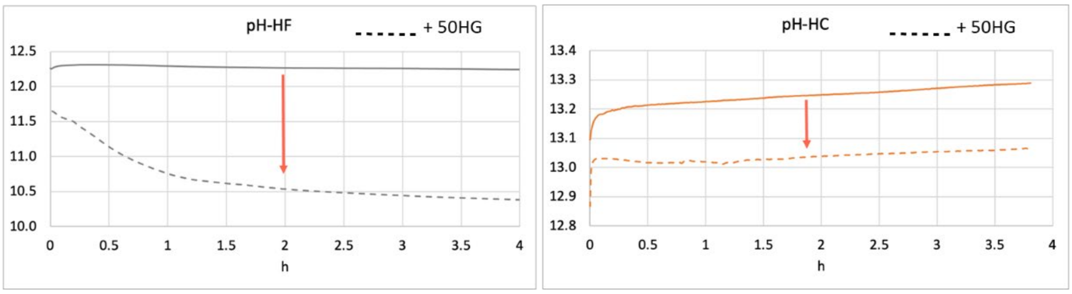


*Fig. 5.3 pH evolution in time for an HF (left) and HC (right) suspensions at w/c=2 with (dashed line) and without (solid line) 50% HG. Arrows represent the decrease of pH due to HG addition.*

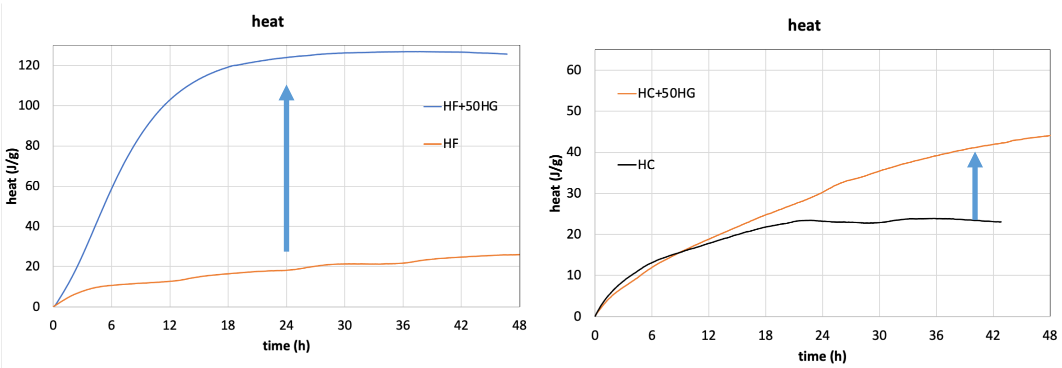


*Fig. 5.4 Cumulative heat evolution in time for an HF (left) and HC (right) pastes at w/c=0.4 with (upper line) and without (lower line) 50% HG. Arrows represent the increase of heat due to the HG addition.*

For both techniques, a direct comparison can be made between the suspensions/pastes with and without HG. For both hydrated cements, the addition of 50% HG causes a pH reduction due to the precipitation of ettringite (and the subsequent reduction of hydroxyl ions). The pH reduction in the case of HF is five times higher than that of HC, in agreement with the increased ettringite formation evidenced by in situ XRPD.
The cumulative heat evolution of HF paste increases significantly when 50% HG is added, starting immediately after water contact and reaching a plateau after one day. This result, together with that of in situ XRPD, suggests that HF+50%HG paste forms secondary ettringite continuously during the first day of hydration. On the other hand, HC+50%HG paste shows slower heat development kinetics. The first increase in cumulative heat is visible after ca.1 day, with an overall increase after 42 hours five times smaller than that of HF.

Conclusions and Perspectives

This study investigated the chemical mechanisms leading to the formation of secondary ettringite in gypsum/cement mixtures. The results show that when an excess of gypsum is added to the HF system, the formation of secondary ettringite is very rapid and ends within the first day of hydration. This result can be related to the expansion test (presented later in WP9), whereby at longer times Fondu cement rather shows shrinkage (both in Le Chatelier rings and prisms). In HC, on the other hand, a low amount of ettringite is formed during the first day in the presence of HG. The process is significantly slower than in HF, but continues over time, potentially creating long-term durability issues.
The perspective of this work is to make the same analysis on a classic OPC (hydrated Der Blaue HB) and follow the three cement (HB, HF, HC) secondary hydration by ex-situ XRPD (with internal standard) to quantify the amount of secondary ettringite which forms at longer times (i.e, months).

**References**

Bollmann, K. 2000. Ettringitbildung in nicht wärmebehandelten Betonen.

Neville, A. 2004. The confused world of sulfate attack on concrete. Cement and Concrete Research, 34, 1275-1296.

Acknowledgments

These tests were conducted at the University of Padua (CiRce center) in collaboration with Prof. MC Dalconi and Dr. Bellotto.

**Alkali-Activated Binders (AAB): solid properties, role of calcium ions and PCE compatibility.**

In the previous report (3rd year, Project 2b, WP5) and in a related article (Liberto et al., 2022), we demonstrated how the addition of both calcium ions (via $CaCl_2$) and a PCE-based superplasticizer can change the fresh properties of AAB pastes, by increasing their workability. The natural successive step consists in producing solid AAB mortars optimizing the amount of both $CaCl_2$ and PCE to maximize the compressive strength.

Materials and Methods

The formulation of our AAB binder was maintained as in the previous study, and consists of (by weight): 91.5% of GGBS (Ground Granulated Blast-furnace Slag, Ecocem), 5% of $Na_2CO_3$, and 3.5% of $Ca(OH)_2$. To prepare AAS mortars, 30% by volume of standard sand (1-2 mm) was added. Distilled water with and without $CaCl_2$/PCE was used as the liquid fraction. The water to binder ratio was then optimized to obtain the best fresh and solid properties. The latter were investigated with the help of a Zwick 250 kN testing machine after 1, 7, 14, 28-day for AAS prisms of 2x2x8 $cm^3$ and 4x4x16 $cm^3$. The AAB mortars at lower water to binder ratio (w/b) needed to be vibrated during the pouring phase into the prisms, due to their low workability.

Results and Discussion

We have shown that the lowest w/b ratio at which AAS mortars can be mixed depends on the quantity of $CaCl_2$/PCE added to the distilled water. Overall, the $CaCl_2$ was varied from 20 to 100 mM and the PCE from 0.3 to 0.9 % (by weight of binder). The optimum was found in the combination of 50 mM of $CaCl_2$ and 0.9 % of PCE, enabling a w/b of 0.345. In contrast, the minimum w/b ratio reachable for pure distilled water and distilled water with 50 mM of $CaCl_2$ is 0.38 (Fig. 5.5).

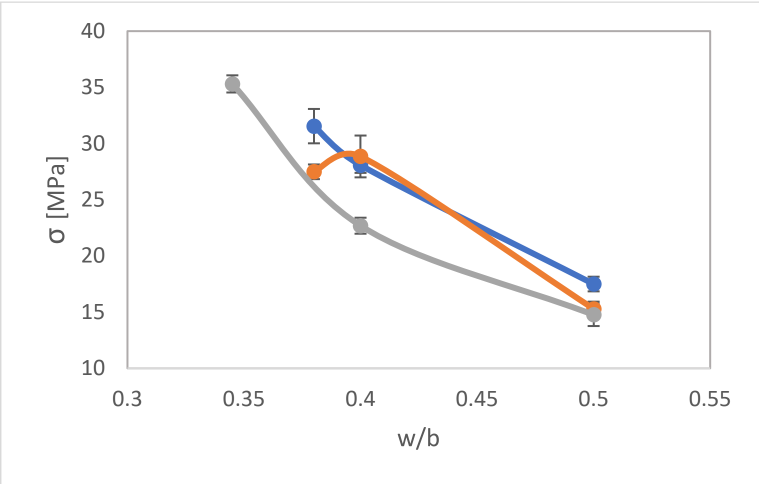


*Fig.5.5 Compressive strength as a function of the w/b ratio of AAB mortar prisms after 28 days, prepared with only distilled water (blue), adding 50 mM of $CaCl_2$ (orange) and adding both 50 mM of $CaCl_2$ and 0.9% of PCE (by weight of binder).*

The addition of PCE in combination with $CaCl_2$ has several benefits. First, it reduces the w/b ratio with a significant increase of the 28-day compressive strength up to 35 MPa. Second, the workability is ameliorated, reducing the problem of compaction during the placement phase in the prisms. The lack of compaction can damage the sample in the hardening phase, and results in lower compressive strengths at longer testing times, as can be seen for the sample with only 50 mM of $CaCl_2$ (orange line in Fig 5.5). The latter was behaving like a thick paste in comparison with the ones without $CaCl_2$ and made the vibration insufficient to ensure full compaction, resulting in a substantial reduction in compressive strength at longer times (28-day). The sample with $CaCl_2$ and PCE has a slower compressive strength development (as in OPC) for the lower w/b (0.4 and 0.5).

We can then expect that at longer times the compressive strength can exceed the 35 MPa.
For our AAB mortar optimized composition (w/b=0.345, 50 mM of $CaCl_2$, and 0.9 % of PCE) different storage conditions were studied. After one day, the prisms were demolded and cured: (a) in contact with the atmosphere, (b) in vacuum-sealed plastic bags, and (c) under water (at room temperature). The time evolution of the compressive strength for the different storage conditions is shown in Fig.5.6. Fig 5.7 shows pictures of the prisms stored in air after 28-day.

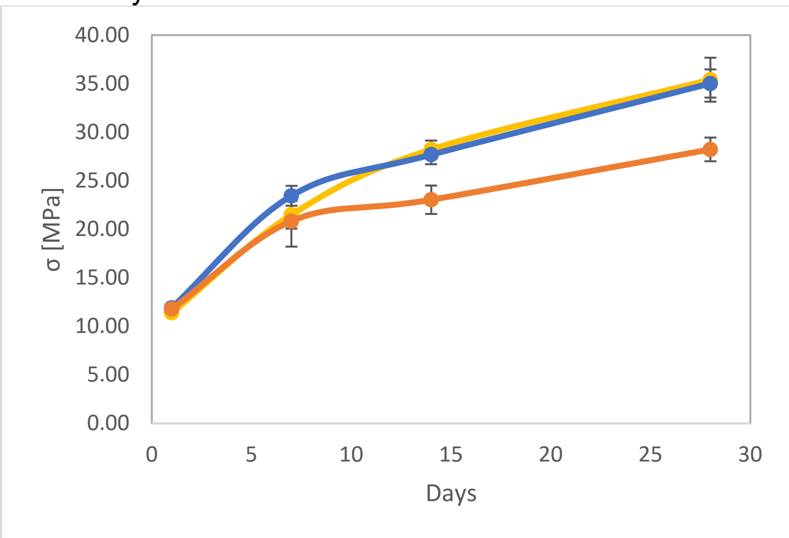


*Fig.5.6 Compressive strength as a function of time of AAB mortar prisms at w/b of 0.345 prepared adding both 50 mM of $CaCl_2$ and 0.9% of PCE (by weight of binder) at different storage conditions: air (yellow), vacuum (blue), and under water (orange).*

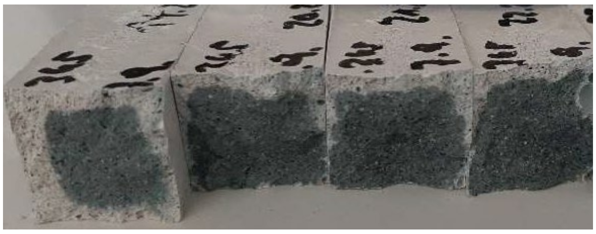

*Fig.5.7 AAB mortar prisms after 28 days prepared at w/b of 0.345 prepared adding both 50 mM of $CaCl_2$ and 0.9 % of PCE (by weight of binder)stored in air.*

The evolution of compressive strength with the three different storage conditions is similar in the first week of curing. For longer times, samples stored in water show a lower compressive strength than the other two storage conditions. Therefore, the contact with water seems to degrade the samples, probably due to a dissolution of the slag portion in the surrounding water. One solution may be to saturate the storage water with portlandite. This difference does not seem to be directly related to the different coloration of the sample. In fact, the presence of sulfur in the slag gives the sample a classic blue/green color. Once the material is in contact with air, its iron-sulfur compounds oxidize and turn the green/blue color into white. This explains why only the sample stored in air shows a white ring on the outer perimeter of the sample. Samples under vacuum and water having no contact with air remain colored inside, but their mechanical properties still differ.

Conclusions and Perspectives

This study on the solid mortar properties of AAB in the presence of $CaCl_2$ and PCE validates previous findings in the study of fresh paste properties, showing the potential of solid AAB for low-load applications. More generally, it confirms the key role of SAOS to define the physico-chemical properties of cementitious systems.
The perspective of this work is to extend the study to durability tests (e.g. shrinkage and longer compressive strength tests). The effect of PCE over time on AAB pastes will also be analyzed. In addition, the development of the early hydration product will be studied by means of XRD and calorimetry, similar to the study carried out for ISA.

References


Purdon, A. O. Improvements in processes of manufacturing cement, mortars and concretes. British Patent GB427 1935, 227
Buchwald, A.; Vanooteghem, M.; Gruyaert, E.; Hilbig, H.; De Belie, N. Purdoce-543
ment: application of alkali-activated slag cement in Belgium in the 1950s. Materials544
and Structures 2015, 48, 501–511
Liberto, T.; Bellotto, M.; Robisson, A. Small oscillatory rheology and cementitious537
particle interactions. Cement and Concrete Research 2022, 157, 106790


Acknowledgments


This report contains data selected from the master thesis of Christian Aschauer: “Investigation of sustainable cement (AAB) fresh and solid properties” (TU Wien repository).


## AP6: Interfaces between old material and new concrete: Bond strength in sloped floors and influence of angle on failure due to drying shrinkage

### Introduction

Previous studies investigated the effects of overlay properties, interface conditions, external environmental conditions, and boundary conditions on the structural performance and durability of concrete-concrete composites subjected to drying shrinkage (Li & Li, 2006; Santos & Julio, 2011). Despite advances made in understanding the drying shrinkage of non-sloped concrete-concrete composites, there are still standing questions regarding the crack formation, as well as bond failure, in sloped concrete-concrete composites. Furthermore, numerous shrinkage and creep prediction models have been developed based on extensive experimental datasets. Although these models have been widely and successfully used, most of the finite-element (FE)-based studies used an analytical or semi-analytical approach to take shrinkage and creep behavior of concrete into consideration. These approaches, in most cases, employed a heat transfer analysis, missing factors contributing to shrinkage and creep.
Given the outlined research gaps and questions, the current study established a high-fidelity computational model validated with experimental tests to evaluate sloped, double-layer concrete systems under drying shrinkage. For this purpose, three-dimensional FE simulations were performed. The shrinkage strain and creep coefficient of concrete were

incorporated as a function of time based on the criteria of the empirical American Concrete Institute model (ACI 209.2R-08, 2008). The simulation scenarios under consideration systematically cover the effects of key overlay properties and interface conditions, such as overlay geometry (thickness and slope), overlay material properties, and interfacial degree of restraint. The outcome sheds light on the optimized combinations of overlay geometries and interfacial conditions required to enhance the short- and long-term performance of concrete-concrete composites.

## Modelling and validation

### Numerical model

The Abaqus software package (2021) was used in this study. The concrete overlay was modeled with a length of 5 m and a width of 2 m. The overlay length was selected long enough (greater than 2 times of the width) to account for the continuity of the overlay. The thickness and slope of the overlay were varied between 20 and 200 mm, and 0 and 10% slope, respectively. The overlay crowned surface slopes from both sides of the centerline. The substrate length was 8 m with a width of 4 m and a constant thickness of 200 mm. Due to the symmetry of the models, a quarter of the described concrete-concrete composites were modeled.
The numerical details of the model are described in the long report.

*Tab. 6.1. Experimental results of concrete properties at 28 days*

| Properties | Value | |
|---|---|---|
| | NC | UHPC |
| Tensile strength (MPa) | 3.6 | 8.3 |
| Compressive strength (MPa) | 63.4 | 134.3 |
| Elastic modulus (GPa) | 26.3 | 36.2 |
| Density (kg/m$^3$) | 2400 | 2500 |
| Poisson’s ratio | 0.2 | 0.2 |

### Drying shrinkage simulation

The empirical ACI 209 shrinkage and creep model was employed to simulate the shrinkage strain and creep of concrete as a function of time (ACI 209.2R-08, 2008). Table 2 lists the coefficients and correction factors used in the FE simulations. The age of concrete at the start of drying and loading was set to 2 days. In this study, the development of drying shrinkage was considered during the first three months of casting so that the time period of analysis was set at 9 × 106 seconds (104 days). All others details are described in the long report and the publication.

*Tab. 6.2. Correction factors for shrinkage strain and creep coefficient based on ACI 209 model*

| Correction factor | Value | |
|---|---|---|
| | Shrinkage | Creep |
| Initial moist curing | 1.13 | - |
| Age of loading | - | 1.15 |
| Ambient relative humidity | 0.69 | 0.8 |
| Member size factor | 0.33 | 0.67 |
| Slump factor | 1.03 | 1.05 |
| Fine aggregate factor | 1 | 1 |
| Cement content factor | 0.97 | 1 |
| Air content factor | 0.99 | 6 |

| | | |
|---|---|---|
| Time ratio (α, ψ) | 0.85 | 0.6 |
| Time ratio (f, d) | 35 | 15 |
| Ultimate shrinkage strain | 1.3 | - |
| Ultimate tensile creep | - | 1.8 |
| Ultimate compressive creep | - | 1.4 |

Validation

To validate the developed FE models, the structural performance of a concrete-concrete composite model was compared to the experimental results reported by (Li & Li, 2006). Similar material properties, geometry and boundary conditions were employed in the model. Figure 2 compares the end corner delamination height of the overlay in the model with the data measured experimentally, supporting the validation of the model used here.

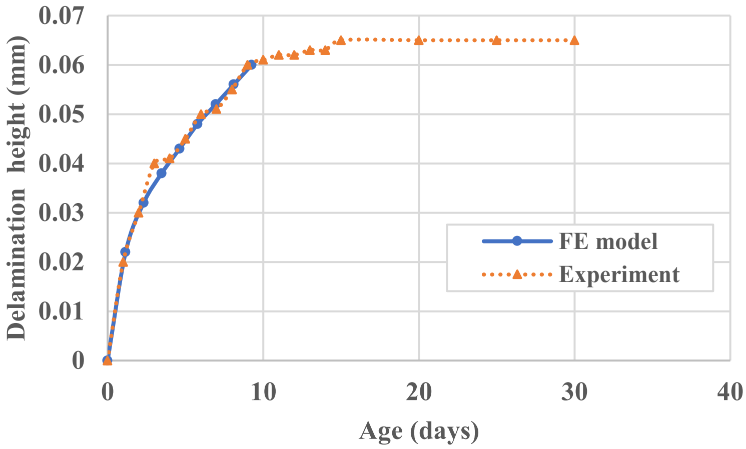


*Fig. 6.2 Comparison of the FE model results with the experimental test data recorded for the corner delamination height in concrete-concrete composites over time*

**Numerical analysis and Results**

Overlay cracking and interface debonding make up a majority of failures in concrete-concrete composites. Therefore, the emphasis of this study is on evaluating the occurrence of these two types of failure, as a function of overlay geometry (thickness and slope), overlay material properties, and interfacial degree of restraint (normal and shear stiffness). Figure 3 show the typical 3D stress distribution and deformed shaped of the concrete overlay subjected to the restrained drying shrinkage.

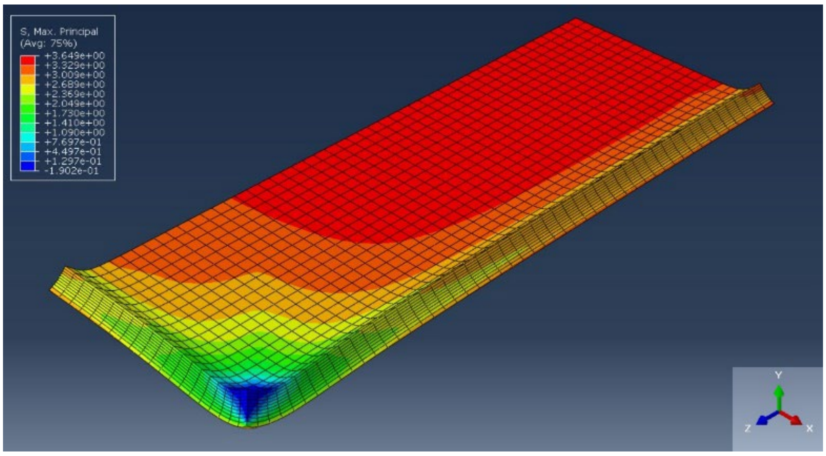

*Fig. 6.3 Typical 3D deformed shape of the overlay in the FE model subjected to restrained drying shrinkage. The contours represent the maximal principal stress before damage initiation. Deformations are amplified by a factor of 3000 for visualization purposes.*

<u>Thickness</u>

The concrete overlay thickness varies depending on the purpose of the application, overlay material properties, and field limitations. Thus, based on the reported values in the literature, a broad range of thicknesses, between 20 and 200 mm, was considered in this study. Figure 4 shows the overlay cracking and interfacial debonding corresponding times.

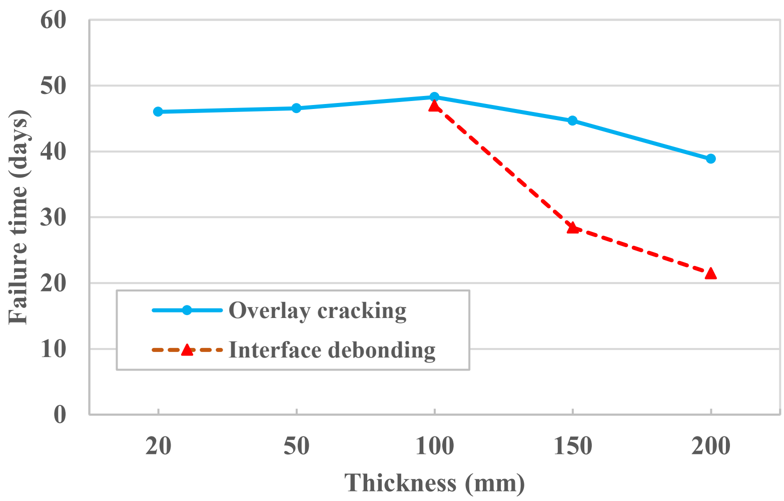


*Fig. 6.4 Overlay drying shrinkage cracking and interface debonding corresponding times as a function of overlay thickness*

The drying shrinkage cracking in overlays with a thickness up to 100 mm was initiated from the center part of the overlays where the induced tensile stress was highest. However, further increasing the thickness resulted in the shift of cracking location to the end corners of the overlay. To compare the stress evolution in overlays with different thicknesses, the stresses induced by the restrained drying shrinkage are plotted in Figure 5 and Figure 6. Results show that in thick overlays, the interfacial normal stresses in end corners exceeded the thresholds earlier than the center part, resulting in a faster occurrence of debonding and development of plastic strains. On the other hand, in thin overlays where the differential shrinkage deformation between the bottom and the top overlay surfaces was not remarkable, the induced tensile stress was concentrated in the center part of the overlay, and therefore, surface cracking was the predominant type of failure.

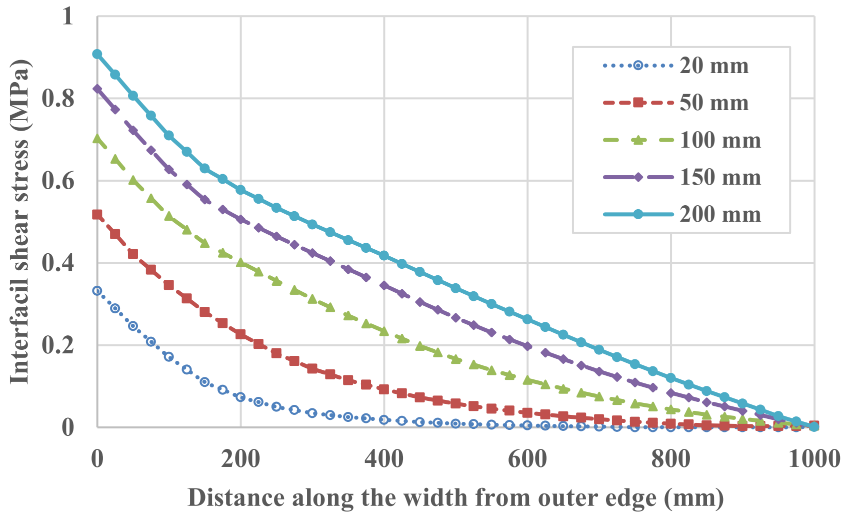


*Fig. 6.5 Distribution of interfacial shear stress along the width of concrete overlays with thicknesses from 20 to 200 mm*

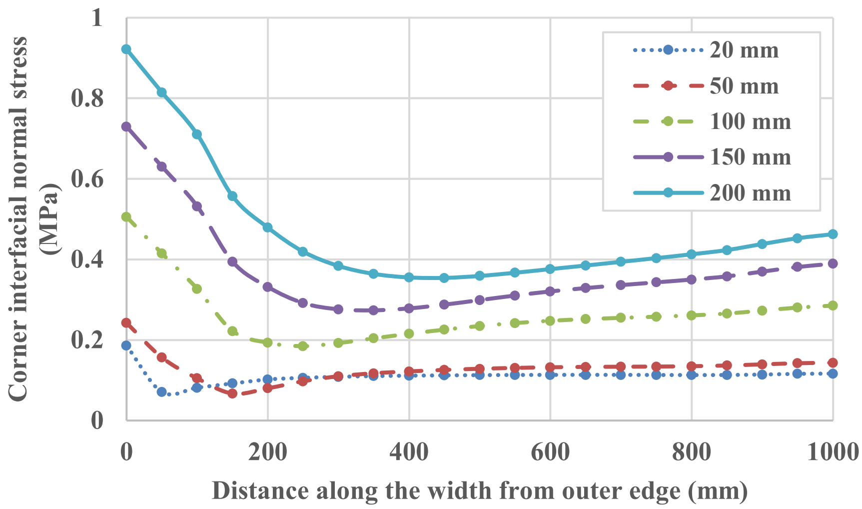


*Fig. 6.6 Distribution of corner interfacial normal stress along the width of concrete overlays with thicknesses from 20 to 200 mm*

<u>Slope</u>

To evaluate the effect of slope in various applications, the overlay cross slope up to 10% was considered with crowned surfaces such that the overlay surface slopes from either side of the centerline. Figure 7 compares the corresponding overlay cracking times.

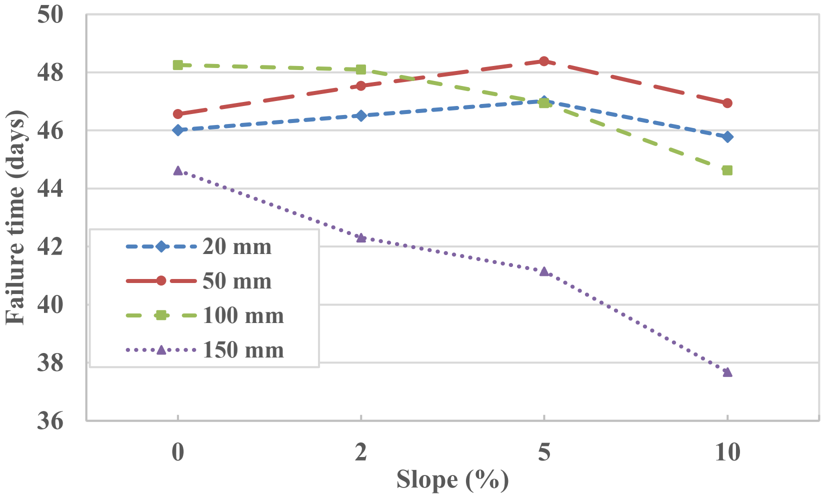

*Fig. 6.7 Overlay drying shrinkage cracking times as a function of overlay cross slope and thickness*

Interfacial stiffness

The non-sloped overlay with a thickness of 100 mm was used in this set of simulations. Greater interfacial stiffness typically induces stronger restraint against overlay displacement along the interface, inducing higher shear and tensile stress. This led to an overlay cracking in composites with an interfacial stiffness greater than 1 N/mm$^3$ (Figure 8).

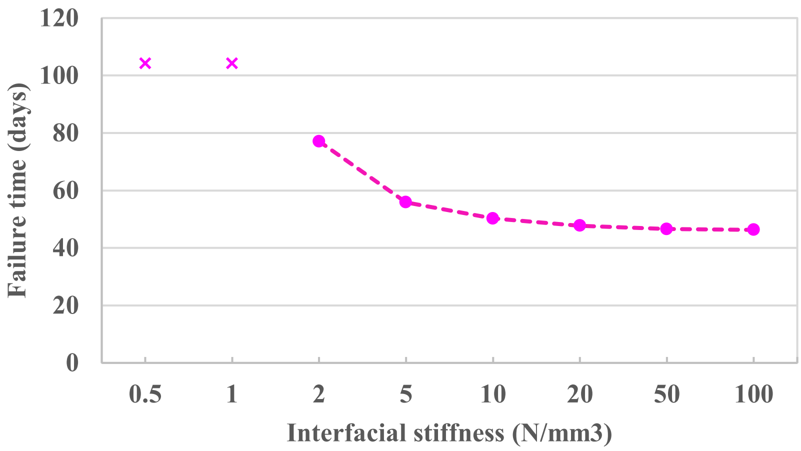

*Fig. 6.8 Overlay drying shrinkage cracking times as a function of interfacial stiffness. The cross marks represent points where failure did not occur during analysis time period.*

Overlay strength

The effect of overlay characteristics was assessed by comparing the structural performance of UHPC with conventional NC. The non-sloped overlay with a thickness of 100 mm was used in the simulation. Figure 9 compares the structural performance of normal and UHPC overlays in concrete-concrete composites subjected to the restrained drying shrinkage.

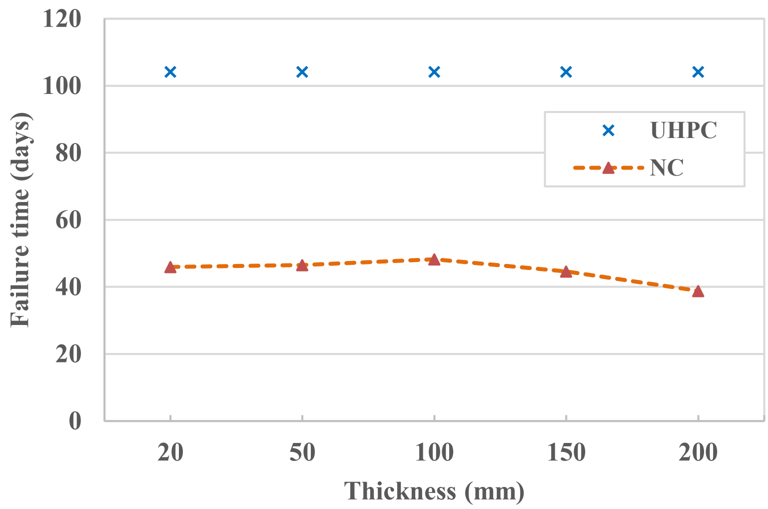


*Fig. 6.9 Comparison of NC and UHPC overlay drying shrinkage cracking times. The cross marks represent points where failure did not occur during the analysis time period.*

Figure 10 shows the interfacial performance of composites including UHPC and NC overlay. As described before, the greater resistance of UHPC against induced tensile and shear stresses leads to the predominant mechanism of stress release through end corner interface delamination. Therefore, the debonding failure occurs (3-10 days) earlier in UHPC overlaid composites than NC ones.

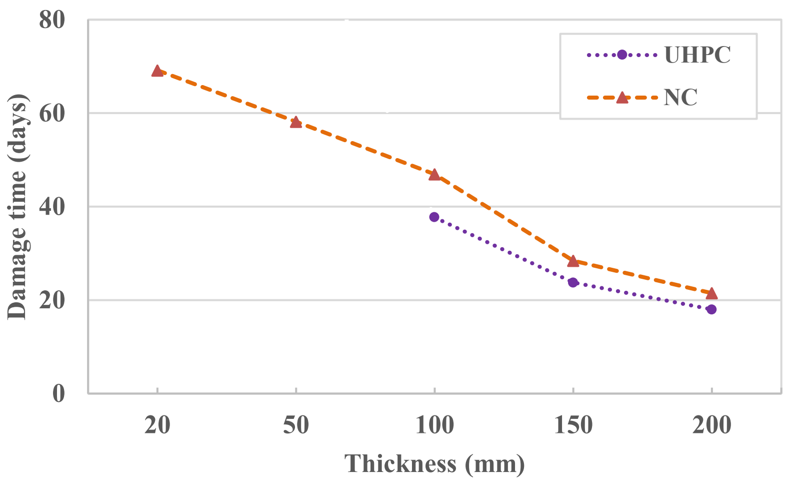


*Fig. 6.10 Comparison of NC and UHPC overlay drying shrinkage cracking times. The cross marks represent points where failure did not occur during the analysis time period.*

## Conclusions

The effects of overlay geometry (thickness and slope), overlay material properties, and interface restraint conditions were investigated in concrete-concrete composites subjected to drying shrinkage. The numerical analysis results showed that the overlay thickness plays a pivotal role in the structural performance of the composites. It was found that there is an optimum point for the overlay thickness (in this study, 100 mm), below

which the overlays are more vulnerable to restrained shrinkage and demonstrate earlier cracking. Employing thicker overlays, on the other hand, was found to result in a significant end corner delamination and hence early-stage interfacial debonding. Consistent with this, the effect of overlay transverse slope was determined to depend on the initial thickness of the overlay such that for the overlays up to 50 mm thick, the overlay crack can be delayed by employing a cross slope up to 5%.
Further increasing the cross slope and employing higher initial thickness would adversely impact the structural performance of concrete-concrete composites through early-age overlay cracking and/or interfacial debonding. Furthermore, the interfacial degree of restraint was found to significantly affect the performance of the double-layer concrete systems such that a sharp drop of 30 days in overlay cracking time was observed upon increasing the interfacial stiffness from 2 to 20 N/mm3. In the case of smoother interfaces, i.e., with an interfacial stiffness less than 2 N/mm3, the overlay restrained shrinkage strain was insignificant to the extent that overlay drying shrinkage cracking did not occur. The type and mechanical properties of the overlay materials also influenced the behavior of the concrete-concrete composites under restrained drying shrinkage conditions. It was found that application of UHPC overlay can delay the overlay shrinkage cracking at least 60 days compared to the NC overlays. However, the end corner interface delamination occurred earlier in UHPC overlays.

Acknowledgments

This work was performed in collaboration with Prof. Behrouz Shafei, from Iowa State University.

### References

ACI 209.2R-08. (2008). Guide for Modeling and Calculating Shrinkage and Creep in Hardened Concrete. American Concrete Institute, USA.

Daneshvar, D., Deix, K., & Robisson, A. (2021). Effect of casting and curing temperature on the interfacial bond strength of epoxy bonded concretes. Construction and Building Materials, 307, 124328.

Li, M., & Li, V. C. (2006). Behavior of ECC-concrete layered repair system under drying shrinkage conditions. In Restoration of Buildings and Monuments (pp. 143–160).

Santos, P. M. D., & Julio, E. N. B. S. (2011). Factors affecting bond between new and old concrete. ACI Materials Journal, 108(4), 449–456.

## AP7: Device for the measurement of infiltration

### Introduction

Samples prepared in the last year and described in the “Year 3 report” were prepared with the focus of testing their injectability. This year, the hardened samples, corresponding to samples for which the slurry was poured from the top, with aggregates previously saturated in water, were machined into cubes. The density of the light weight concrete was measured and the compressive strength tested.

### Materials and methods

For the first trial, low strength Liapor beads 4-8 mm and 8-16 mm were used. No optimization of Liapor bead selection, bead packing or cement design was performed for these preliminary tests. Lightweight concrete samples tested here were prepared with the cement slurry poured from the top, and with beads (lightweight aggregates) previously saturated in water. This manufacturing process was shown in last year report

to lead to large defects. The samples were none-the-less cut into cubes and tested to obtain a base line, from which we will optimize the next series.
Cubes of 60x60x60 $mm^3$ were cut out of 4 concrete samples: Serie B was prepared with Liapor beads 4-8 mm and series A, C and D with Liapor beads 8-16 mm.
Samples were crushed with a ZwickRoell 250 kN testing machine, see Fig. 7.1.

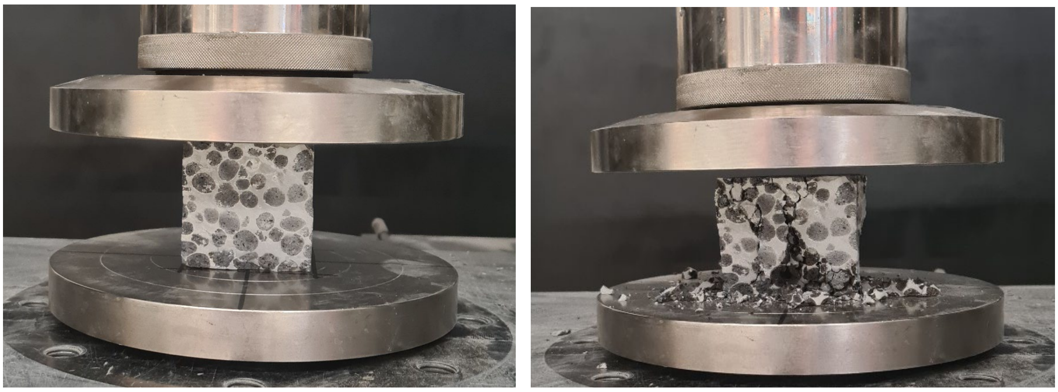

*Fig. 7.1: Compressive strength measurement. Left: initial sample, Right: post-test sample.*

**Results**

All results are plotted with compressive strength as a function of density, see Fig 7.2. The density of samples ranges from 1018 to 1366 $kg/m^3$ and the compressive strength from 3.9 to 12.3 MPa. Dispersion is very large inside a same series, highlighting the low quality of producing light weight concrete from pouring cement slurry from top on expanded clay beads previously saturated with water. As described in the previous report, water accumulated in pocket creating weak zones in the column.
Using all results, a linear regression can be fitted, confirming that strength typically inversely correlates with density. The equation of the fitted curve is:

Compressive strength (MPa) = 0.0214 x Density ($kg/m^3$) - 17.56

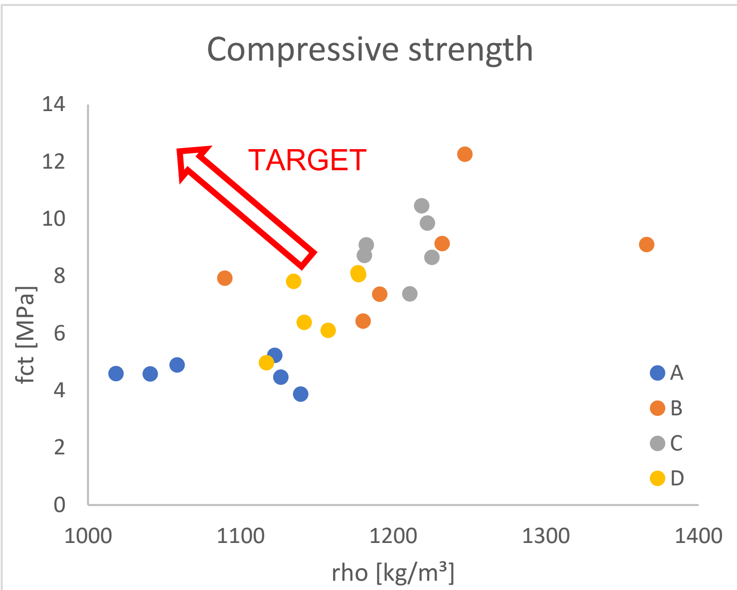


*Fig. 7.2: Compressive strength versus density for 4 low density concrete made of low strength Liapor beads (Series B: 4-8 mm, Series A, C and D: 8-16 mm).*

**Conclusion**

Lightweight concrete samples prepared by pouring cement on top of water saturated low-strength Liapor beads gives unsatisfactory strength (maximum 12 MPa) [1], and shows rather high dispersion in both density and strength. This result was expected following last year report but gives nonetheless a baseline for further optimization.

**References**

[1] Elshahawi, M., Hückler, A. and Schlaich, M., 2021. Infra lightweight concrete: A decade of investigation (a review). Structural Concrete, 22, pp.E152-E168.

## AP9: Recycled aggregate concretes: recipe optimization for concrete made with recycled concrete based on packing & measurement of volume changes during internal sulfate attacks

### Recipe optimization for HP-concrete made with recycled HP-concrete based on packing

This research aimed at studying the feasibility of using recycled concrete as aggregate or binder (RA), obtained from demolished concrete, in the production of new high-performance concrete (HPC). The design of HPC largely relies on optimizing the packing of solids, and replacing the constituents of HPC with recycled material impacts the size distribution which in turns impacts the packing density of the particles in the mixture. Here, the packing density of particles is defined as the ratio of the solid volume of the particles to the bulk volume occupied by the particles. Because the solid content (i.e. packing) affects the rheological and mechanical properties of the concrete, all recipes of recycled concretes tested here were optimized using a packing model. In fact, the basic proportioning strategy is to design the granular mixture with minimum porosity. Several theoretical packing models were developed to determine the porosity of the granular mixture based on the particle size distribution of the constituents. In 1959, Schwanda developed and published a mathematical method, which can be used for the determination of the void content of any grain mixtures, of which the grain distribution is given [1]. This model has already been proved to be suitable for the void calculation of various mixtures including concrete mixtures. Considering this, we investigated the effect of adding recycled particles on the packing density of the mixture using the Schwanda model. All possible combinations and mix designs were considered and the main purpose was to optimize the mixture, achieving a packing density as high as possible. After grinding the old concrete in the lab, and considering the size of quartz sand particles was in the range of 0.1 to 0.5 mm, we decided to select three different sizes of RA consistent with that aforementioned range as follows:

- 0.125-0.25 mm
- 0.25-0.5 mm
- 0.5-1 mm

To calculate the packing density, we first measured the particle size distribution (PSD) of quartz sand as well as RAs using *Mastersizer 3000 Malvern Panalytical* as shown in Figure 1.

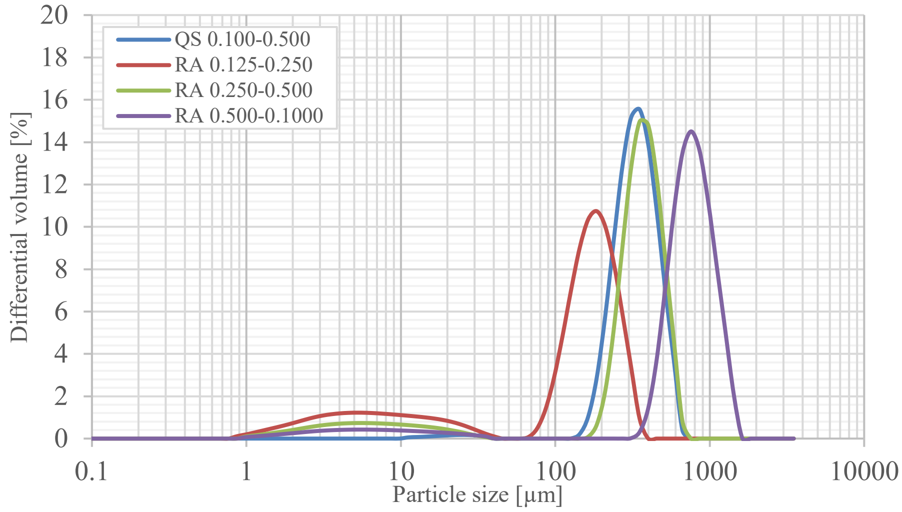


*Fig. 9.1 Particle size distribution of quartz sand and recycled aggregates with different sizes*

In this study, two replacing approaches were employed:

- Full replacement (100%) of quartz sand with recycled aggregate (RA)
- Partial replacing of quartz sand with RA based on packing density results

Considering these approaches, we assessed all the possible combinations for the full and partial replacement as presented in Tables 1 and 2, respectively. The higher the packing density (PD%), the denser the microstructure of the concrete, resulting in greater mechanical properties and more durable performance.

*Tab. 9.1 The packing density of the aggregate mixture in case of complete replacement (100%) of quartz sand with recycled aggregate. Mass fraction is calculated based on the total mass of solids.*

| **Component 1** | **Component 2** | **Component 3** | **Mass fraction (%)** | | | **PD (%)** |
|---|---|---|---|---|---|---|
| | | | **C1** | **C2** | **C3** | |
| QS 100-500 | - | - | 100 | - | - | 61.2 |
| RA 125-250 | - | - | 100 | - | - | 70.7 |
| RA 250-500 | - | - | 100 | - | - | 73.2 |
| RA 500-1000 | - | - | 100 | - | - | 77.6 |
| RA 125-250 | RA 250-500 µm | - | 0 | 100 | - | 73.2 |
| RA 250-500 | RA 500-1000 µm | - | 16 | 84 | - | 79.6 |
| RA 125-250 | RA 500-1000 µm | - | 12 | 88 | - | 79.6 |
| RA 125-250 | RA 250-500 µm | RA 500-1000 | 12 | 1 | 87 | 79.6 |

*Tab. 9.2 The packing density of the aggregate mixture in case of partial replacement of quartz sand with recycled aggregate. Mass fraction is calculated based on the total mass of solids.*

| **Component 1** | **Component 2** | **Component 3** | **Component 4** | **Mass fraction (%)** | | | | **PD (%)** |
|---|---|---|---|---|---|---|---|---|
| | | | | **C1** | **C2** | **C3** | **C4** | |
| QS 100-500 µm | - | - | - | 100 | - | - | - | 61.2 |
| QS 100-500 µm | RA 125-250 µm | - | - | 46 | 54 | - | - | 74.3 |
| QS 100-500 µm | RA 250-500 µm | - | - | 35 | 65 | - | - | 75.1 |
| QS 100-500 µm | RA 500-1000 µm | - | - | 0 | 100 | - | - | 77.6 |
| QS 100-500 µm | RA 125-250 µm | RA 250-500 µm | - | 35 | 0 | 65 | - | 75.1 |
| QS 100-500 µm | RA 250-500 µm | RA 500-1000 µm | - | 0 | 16 | 84 | - | 79.6 |
| QS 100-500 µm | RA 125-250 µm | RA 500-1000 µm | - | 0 | 12 | 88 | - | 79.7 |
| QS 100-500 µm | RA 125-250 µm | RA 250-500 µm | RA 500-1000 µm | 0 | 12 | 1 | 87 | 79.6 |

Based on the results, it was found that introducing recycled aggregates (RA) to partially or fully replace natural aggregates may be beneficial in terms of packing density. Indeed, the packing density of the quartz sand was individually 61.2%, but all three different sizes of the RA had greater packing density above 70%. Thus, upon adding RA (fully and/or partially), a denser solid can be achieved. The highest packing density (79.7%) was associated with the full replacement of quartz sand with a combination of two different sizes of RRs, namely RA 125-250 um (12%) and RA 500-100 um (88%).
The effect of RA addition on the packing density of the whole concrete design (considering all solid parts of the HPC mixture, was also investigated. The solid part, in this case, includes the aggregates, the cement, the silica fume, and the quartz powder. As can be seen in Table 3, the packing density of the reference mix was 76.21%, and upon replacing the aggregate part with recycled aggregate coarser than 250 $\mu$m, the whole solid mixture gained a higher packing density.

*Tab. 9.3 The packing density of the solid part of the mixture in case of full/partial replacement of quartz sand with recycled aggregate. Mass fraction is calculated based on the total mass of solids excluding the superplasticizer and consistency holder.*

| **Component 1** | **Component 2** | **Component 3** | **Component 4** | **Mass fraction (%)** | | | | **PD (%)** |
|---|---|---|---|---|---|---|---|---|
| | | | | **C1** | **C2** | **C3** | **C4** | |
| QS 100-500 µm | CEM | Silica fume | QM | 41 | 37 | 7 | 15 | 76.21 |
| RA 125-250 µm | CEM | Silica fume | QM | 41 | 37 | 7 | 15 | 74.02 |
| RA 250-500 µm | CEM | Silica fume | QM | 41 | 37 | 7 | 15 | 76.65 |
| RA 500-1000 µm | CEM | Silica fume | QM | 41 | 37 | 7 | 15 | 79.52 |

Finally, the solid powder was made into a full concrete recipe (see long report) and the fresh properties were also tested and results are presented in Fig. 9.2 and 9.3. Please note that due to the open porosity of the recycled aggregates, additional water (125 mL for 1.7 kg of aggregates) was added to the mix.

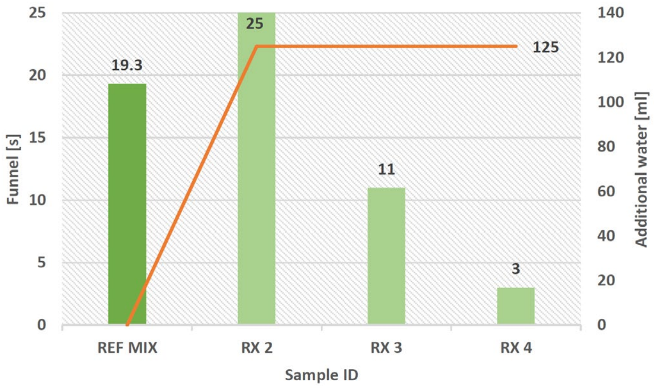


*Fig. 9.2 Funnel flow time for full replacement of sand. Ref mix contains sand, RX2 contains RA 125-250 µm, RX3 contains RA 250-500 µm, RX4 contains RA 500-1000 µm*

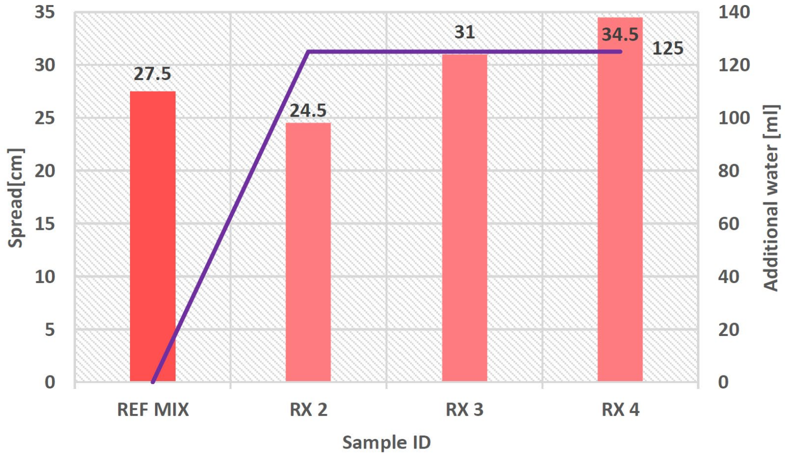


*Fig. 9.3 Cone spread for full replacement of sand. Ref mix contains sand, RX2 contains RA 125-250 µm, RX3 contains RA 250-500 µm, RX4 contains RA 500-1000 µm*

## References

[1] Schwanda, F., 1959. Der Hohlraumgehalt von Korngemischen. *Ein Vergleich rechnerisch gewonnener Werte mit versuchsmäßig ermittelten. beton*, *9*, pp.12-19.

Acknowledgments

This report is based on the master thesis of Valdrin Maliqi: “Use of recycled UHPC aggregates in UHPC” (TU Wien repository).

## Expansion measurements due to ISA in RC

Quantifying the expansion for excess of gypsum in recycled concrete (RC) is crucial to prevent internal sulfate attack (ISA), as explored in the last report (3rd year, WP5+WP9). This study aims to quantify the effect of ISA on various types of cement in order to bring greater insight into the early deterioration mechanisms (which can result in serious structural damage), especially risky when RC are used.

In our preliminary study, various methods were employed, such as: prism length variation, Le-Chatelier expansion rings, and an oedometer cell integrated into a compression device. Key variables for ISA were varied such as: water/cement ratio, cement type, cement hydration state, curing and ambient environmental conditions, gypsum content, and fineness.
One of the open challenges was to properly measure the expansion in Le-Chatelier ring, for several excesses of gypsum (i.e., 0, 5, 10, 25, and 50%).
The confinement was then secured to avoid vertical expansion, introducing the ring in between two plexiglass plates, and tightening the two ends with screws (passing through the plexiglass prisms), as shown in Fig. 9.4.

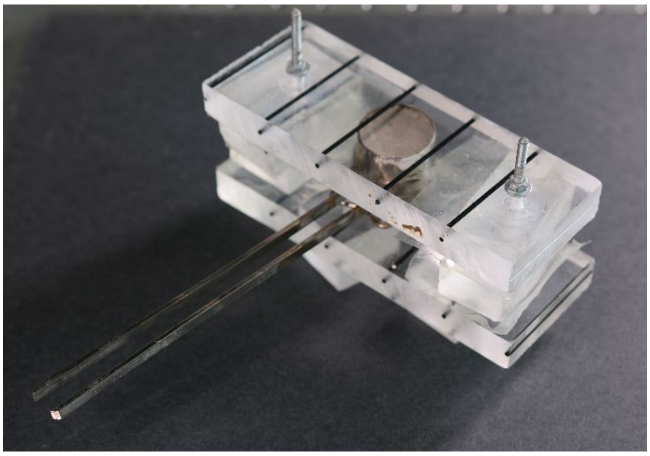

*Fig. 9.4: Le-Chatelier ring confined setup to avoid vertical expansion.*

In the current study, we have also substituted the Supracem, used in our previous campaign, with another aluminum-rich cement with a well-known composition: Ciment Fondu (Lafarge). We then tried to study the expansion of the Hydrated Fondue (prepared following the same protocol as in the 3rd year report, WP5+WP9) with an increased amount of hydrated gypsum (HG) with Le-Chatelier ring and the new confinement setup.
The different HF+HG formulations with a low amount of HG (i.e., 0, 5, 10, 25%) showed a low consistency (fluid rather than pasty) for the same water to solid (i.e., hydrated cement powder) ratio in comparison with the previously tested cements (Blaue and Contragress, 3rd year report, WP5+WP9). This led to leakage when loading the sample into the ring.
The sample HF+50%HG instead had a more appropriate consistency but, after 1-day setting, showed shrinkage, losing contact with the ring, making the confinement fail. Moreover, this sample degraded over time, and even after 50 days, it did not reach a stable solid state.
Hydrated Der Blaue and Contragress (HB and HC) were also tested with a lower amount of HG (i.e., 0, 5, 10, 25). In the previous study, only 50% of HG was added to the hydrated cements in the Le-Chatelier ring.
Similar consistency issues occurred with HC, making confinement before curing once more very difficult and compromising the reliability and reproducibility of the results. Only the HB showed proper confinement even without HG. The expansion of the HB+HG series (0-25%) was then not enough to give a clear trend.

During this more extensive study, we defined the limits of Le-Chatelier ring. This setup works only when the hydrated paste shows a high consistency and stability. The estimation of expansion is accurate only when a high excess of gypsum (i.e., 50%) is added to previously hydrated cement. Due to these experimental limitations, no temperature effects were possible to explore.
To the present day, the prisms with different fresh cement types (i.e., not hydrated and milled as in Le-Chatelier) and excess of gypsum (0, 5, 10%, 3rd year report, WP5+WP9), continue to show no expansion after almost two years of aging. Length measurements conducted over a few months showed shrinkage in Ciment Fondu prisms, prepared following the same protocol of other cements (i.e., Blaue and Contragress).
Extensive studies were also made to set the oedometer to test our samples at higher temperatures. All calibration tests made with different confined materials (i.e., plexiglass, firestone..) at high temperatures (60-80°C) failed, resulting in misleading results. No explanation was satisfactorily provided by the manufacturer.
After several tests with the above devices, we came to the conclusion that the hydrated cements pastes should be tested with a home-made confined swelling setup, equipped with temperature control. This in order to estimate the 3D expansion of the sample even in a less aluminum-rich cement or when a lower gypsum content is added.

Acknowledgments

This report is based on the master thesis of Hossam Al Daffaie (manuscript in progress).

## 3. Project team and cooperation

- Are there significant changes in the project team (internal key staff and external partners/third parties)?
- Address changes in the division of labour.
  Are there any effects on the cost / financing structure and the target?

## 4. Economic and scientific exploitation

- Describe the exploitation and / or redistribution activities carried out so far.
  Is exploitation possible?
- List publications, dissertations, theses and any patent applications, which have arisen from the project.
- What further R&D activities are planned?
- How will the prototypes created in the project be further used?

Peer-reviewed publications and books

D. Daneshvar, K. Deix, A. Robisson, Effect of casting and curing temperature on the interfacial bond strength of epoxy bonded concretes, *Construction and Building Materials*, *307*, p.124328

Daneshvar, D., Deix, K., Robisson, A. and Shafei, B., 2022. Investigation of drying shrinkage effects on sloped concrete-concrete composites. In *Computational Modelling of Concrete and Concrete Structures* (pp. 634-639). CRC Press.

Liberto, T., Bellotto, M. and Robisson, A., 2022. Small oscillatory rheology and cementitious particle interactions. *Cement and Concrete Research*, *157*, p.106790.

FFG-Berichte und Langberichte befinden sich allgemein zugänglich auf der Website der Österreichische Bautechnik Vereinigung

Master thesis (Diplomearbeit)

Aschauer, C., 2022. *Untersuchung der Frisch-und Festigkeitseigenschaften von nachhaltigem Zement (AAB)* (Technische Universität Wien).

Maliqi, V., 2021. *Use of recycled UHPC aggregates in UHPC* (Technische Universität Wien).

Pointner, L., 2021. *Infiltration of cement paste in porous media* (Technische Universität Wien).

Čamber, R., 2021. *Untersuchungen zu Treiberscheinungen in Beton ausgelöst durch rezyklierte Gesteinskörnung.*

Bohl, H., 2021. *Einfluss der Trockenmischdauer auf die Deagglomeration von Silicastaub in UHPC*

## 5. Explanations on costs & financing

- Billing is done directly in eCall or, for projects submitted by Sept. 2015, via Excel. In eCall you will automatically be presented with the right variant for you.
- Please refer to the FFG cost guidelines (www.ffg.at/kostenleitfaden) and tender documents.
- Deviations from the cost plan must be described and justified at this point.

## 6. Project specific special conditions and requirements

- Deal with project-specific special conditions and requirements (according to §6 of the Grant Agreement), if these have been agreed in the Grant Agreement or Contract for Work and Labor.

## 7. Notifiable events

Are there any special events relating to the funded project which must be notified to the FFG (see also Guidelines - Annex to 5.3., 5.3.5), e.g.

- Changes in the legal and economic possibilities of influencing the Recipient
- Insolvency proceedings
- events that delay the performance of the subsidised service, or render impossible
- Further funding for this project